

backscattering-immune, one-way transport and robustness against defects or imperfections, such as photonic quantum Hall insulators [6–11], photonic quantum spin Hall insulators [12–16], photonic quantum valley Hall insulators [17–20], photonic topological Anderson insulators [21–23], and photonic Floquet topological insulators [24, 25]. These photonic systems with nontrivial topology offer unprecedented opportunities for efficient and robust molding of light on a nanophotonic chip and integrated photonics, important for extension and advancement for conventional condensed matter physics and optics based on nontrivial topological photonic states. There are a great number of revolutionary and intriguing topics derived from topological photonics, such as topological bound states in continuum (BIC) [26], topological non-Hermitian skin effect [27–29], topological quantum entanglement [30, 31], and topological microcavity lasers [32, 33]. These advances vastly facilitate progress of communication technology with new functions or improved performance.

In a two-dimensional topological photonic system, valley-dependent edge states emerge at the interface formed by stacking two mirror-inverted valley photonic crystals (VPCs) [17, 18, 34], achieved by breaking the parity-reversal symmetry (PRS). This mimics the quantum valley Hall effect (QVHE). These edge states are protected against intervalley scattering at defects that preserve the C_3 crystalline symmetry. Compared to the photonic quantum Hall effect (QHE) and the quantum spin Hall effect (QSHE), the photonic QVHE offers distinct advantages, primarily due to two factors: (1) valley-dependent spin-split photonic bulk bands resulting from PRS breaking, and (2) the valley degree of freedom (DOF), a binary index that serves as a superior information carrier. Moreover, the photonic QVHE can be readily implemented using all-dielectric materials and fabricated with conventional nanofabrication techniques. Significant progress has recently been made in terahertz on-chip communication. Nanophotonic chips based on the QVHE have been developed and experimentally fabricated, with wireless communication efficiencies continuously improving — for example, reaching 13 Gbps [35], 100 Gbps [36], 160 Gbps [37], and 320 Gbps [38]. Beyond transmission characteristics, researchers have also explored the localization and trapping of topological edge states. For instance, the “topological rainbow” phenomenon [39–42], in which edge states of different frequencies are robustly localized at distinct spatial positions, provides a novel platform for manipulating electromagnetic (EM) wave in integrated photonics. Another important example is the localization of chiral edge states via non-Hermitian skin effects [28]. However, the frequency-dependent localization of topological edge states at specific interfaces remains unexplored and unreported.

To the best of our knowledge, the design and realization

of topological rainbows are mainly based on three principles or approaches: dispersion engineering, synthetic dimensions, and Landau levels. Among these, dispersion engineering is the most widely employed. By combining it with topological properties, the topological rainbow phenomenon can be realized, for instance, by modulating the external magnetic field strength [43], designing structures with gradually varying parameters [44], or introducing graded losses [45]. However, their practical implementation often involves complex fabrication processes, which poses a challenge for photonic integration. On the other hand, considerable research has shown that interface coupling distance [46, 47] and termination geometries or interface stacking types [48, 49] (e.g., zigzag, armchair, and bearded interfaces) serve as key factors for enabling precise control over EM wave frequency. Building on studies of dispersion curves for valley Hall edge states at different interfaces, we propose a topological waveguide structure comprising such interfaces. This approach suggests that the interface itself could be leveraged as a DOF for manipulating EM wave. Compared to previous approaches, this strategy could facilitate the development of integrated photonic devices by simplifying fabrication requirements and enhancing design flexibility.

In this work, we systematically investigated valley Hall edge states at different interfaces of VPCs, such as bearded and armchair interfaces. We theoretically analyzed and demonstrated that the valley Hall edge states at each type of interface possess distinct transmission characteristics. Subsequently, we constructed a U-shaped topological waveguide composed of both bearded and armchair interfaces. Through both numerical simulations and experimental measurements, we achieved and observed frequency-dependent localization and confinement of valley Hall topological states at specific interfaces in the U-shaped waveguide structure. These results thereby offer a potential and feasible platform for manipulating EM wave using interfaces as an additional DOF at the nanoscale. This approach is particularly promising for applications in integrated photonics, such as multi-frequency routers [50] and ultra-compact topological rainbow nanolasers [51].

2 Valley photonics crystals

Figure 1(a) shows a schematic of the all-dielectric VPCs with a honeycomb lattice, composed of alumina cylinders (relative permittivity $\epsilon_r = 7.5$) in air. The VPC has a rhombic unit cell containing two alumina cylinders of different diameters. This diameter inequivalence breaks the primitive PRS and consequently opens a two-dimensional photonic bandgap (PBG) [18, 20, 35]. Figures 1(b1)–(b3) illustrate three types of VPC lattice cells, designated as VPC1, VPC0, and VPC–1, respec-

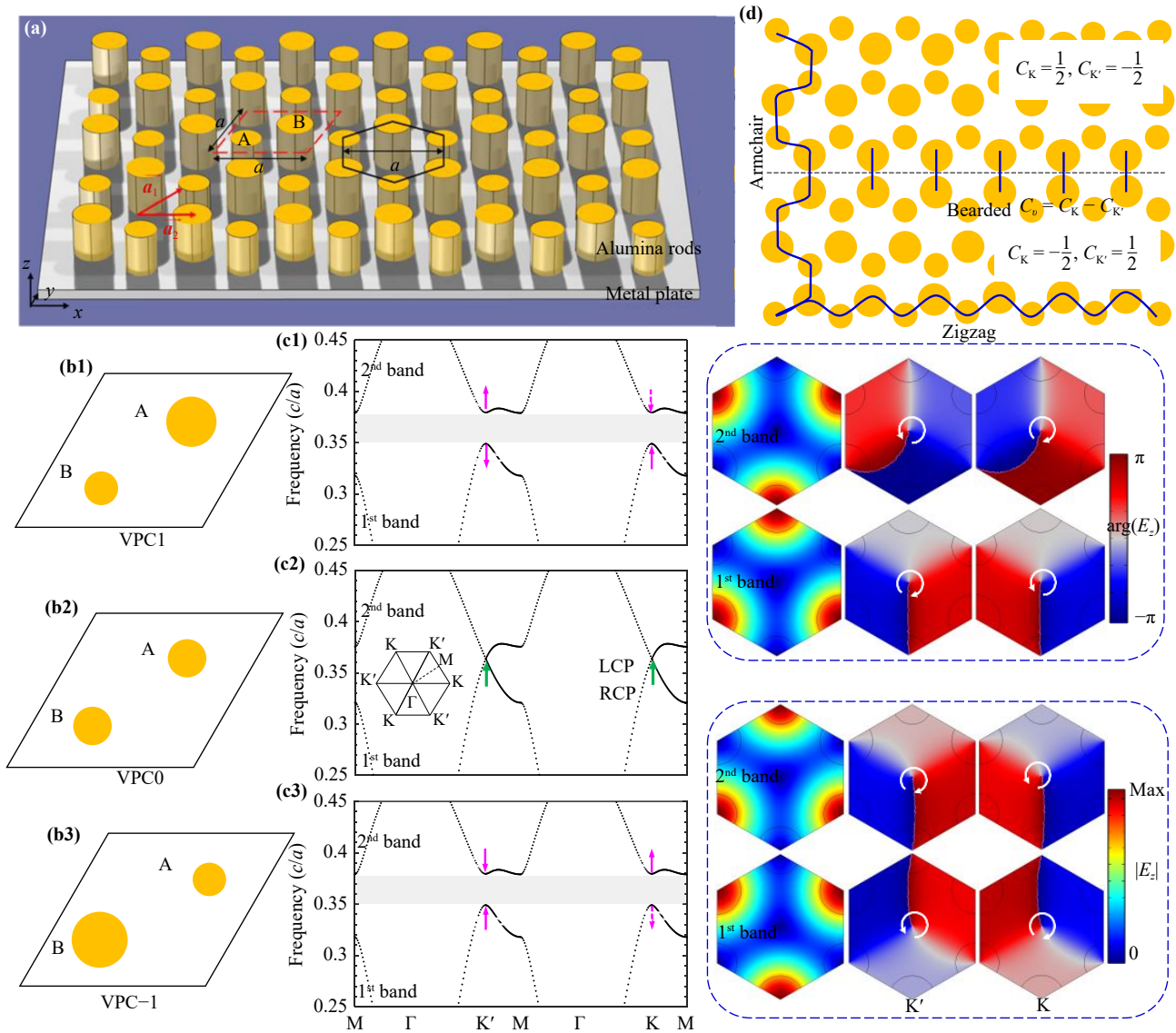


Fig. 1 (a) Schematic of all-dielectric VPCs with honeycomb lattice. Here vectors \mathbf{a}_1 and \mathbf{a}_2 denote the translation vectors and a is the lattice constant ($a = 16$ mm). (b1–b3) Schematic of three kinds of VPCs cell units, VPC1, VPC0, VPC-1 respectively. (c1–c3) Photonic band diagrams in the first Brillouin zone (FBZ), corresponding to (a1–a3), respectively. The right panels denote the electric field amplitude $|E_z|$ and phase distributions of eigenmodes at the K/K' valley in the first and second band respectively. (d) Schematic of the VPCs with honeycomb lattice (array of waveguides), with the three principal edge terminations there of: bearded, zigzag and armchair edges, respectively. Blue lines denote edge shapes.

tively. Their geometric parameters are defined as follows: $d_A = 6/16a$ and $d_B = 5/16a$; $d_A = 2r_0 = 11/32a$ and $d_B = 2r_0 = 11/32a$; $d_A = 5/16a$ and $d_B = 6/16a$. Here, d_A and d_B are the diameters of circles A and B, respectively, and r_A and r_B are their corresponding radii. For VPC1, the radii are $r_A = r_0(1+\delta) = 3$ mm and $r_B = r_0(1-\delta) = 2.5$ mm, with $\delta = 1/11$ defined as the valley-dependent deformation parameter. The photonic band structures for transverse magnetic (TM) modes were calculated by using the finite element method (COMSOL Multiphysics 6.0), as presented in Figs. 1(c1)–(c3). A Dirac cone (indicated by green arrows) is observed in the band structure of VPC0. This

Dirac cone opens when the cylinder diameters become inequivalent, resulting in the appearance of a PBG. Our calculations, presented in the right panels of Figs. 1(c1)–(c3), verify that PRS breaking induces valley-dependent spin-split bulk bands, manifested as opposite valley spins and a strongly localized electric field amplitude at the respective K and K' valleys.

Due to the large separation between the two valleys in \mathbf{k} -space, a valley-dependent topological invariant can be defined. This invariant, namely the valley Chern number, is used to classify the topological states of the different lattices. It is defined as follows:

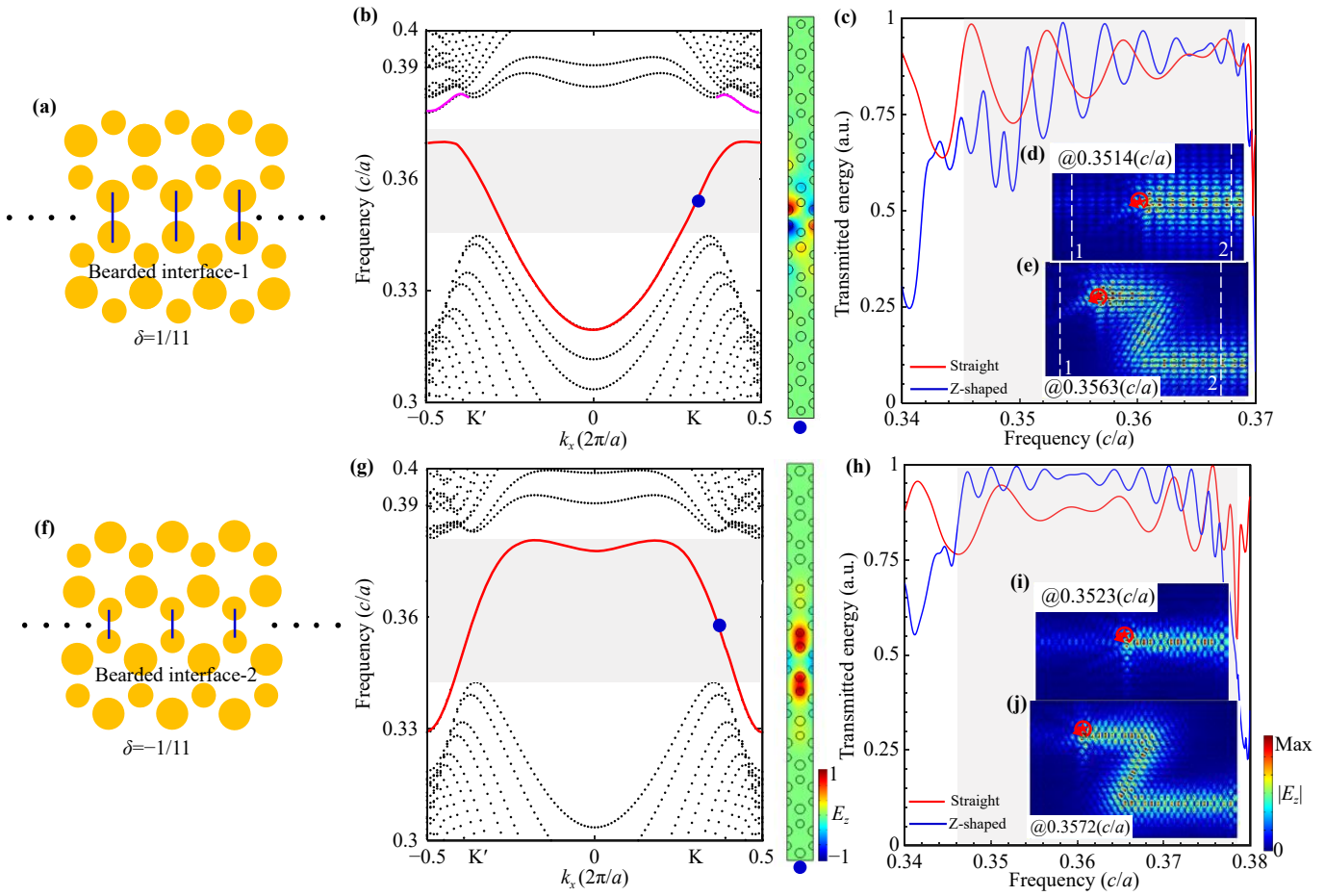


Fig. 2 Valley Hall edge states in the bearded interface. (a, f) Schematic of bearded interface-1 and -2. (b, g) The photonic bulk band diagrams along Γ -K momentum space, where red and pink lines denote topological nontrivial and trivial edge modes dispersion respectively. The shadow indicates the frequency range where only valley Hall edge modes exist. Right panel: valley Hall edge eigenmodes (E_z) marked by blue dot. (c, h) The transmission spectra as a function of frequency in straight and Z-shaped waveguide for the bearded interface-1 and -2. (d, e) and (i, j) Electric field amplitude ($|E_z|$) distributions of valley Hall edge states in straight and Z-shaped waveguide for bearded interface-1 and -2, where red star and circular arrow denote location and polarized direction of chiral source, respectively.

$$C_{K/K'} = \frac{1}{2\pi} \iint_{K/K'} F(\mathbf{k}) d^2\mathbf{k},$$

where $F(\mathbf{k}) = \nabla_{\mathbf{k}} \times \mathbf{A}_n(\mathbf{k})$ and $\mathbf{A}_n(\mathbf{k}) = \langle \mathbf{u}_n(\mathbf{k}) | i\nabla_{\mathbf{k}} | \mathbf{u}_n(\mathbf{k}) \rangle$ are the Berry curvature and Berry connection respectively, and $\mathbf{u}_n(\mathbf{k})$ is the spatially periodic part of the Bloch function for the n th band. Integrating Berry curvatures around different valleys, we further find that the valley Chern numbers are half-integers, that is, $C_K = 1/2$ and $C_{K'} = -1/2$ for the first band, $C_K = -1/2$ and $C_{K'} = 1/2$ for the second band. The differences in the valley Chern numbers across the domain wall, formed by two mirror-symmetric VPCs at the K and K' valleys, are calculated to be $C_v = \pm 1$ ($C_v = C_K - C_{K'}$). According to the bulk-edge correspondence principle [52], these quantized differences guarantee that within PBG a pair of valley Hall edge states exists at the domain wall. In a honeycomb lattice, three principal edge terminations, namely, bearded, zigzag, and armchair (implemented as

arrays of waveguides) [48], give rise to distinct domain-wall configurations, as illustrated in Fig. 1(d). By connecting two VPCs with distinct topological phases, a pair of valley Hall edge states emerges within the PBG: one at the K valley propagates unidirectionally along one direction, while its counterpart at the K' valley propagates unidirectionally in the opposite direction.

3 Valley Hall edge states at different interfaces

For bearded interface-1 [see Fig. 2(a)], the photonic band diagram along wavevector k_x is shown in Fig. 2(b). Within PBG marked by a shadow, a pair of valley Hall edge states emerges at the K and K' valleys and these states propagate in opposite directions along the bearded interface-1. Additionally, there are two pairs of trivial topological edge states (marked by pink curves) gapped

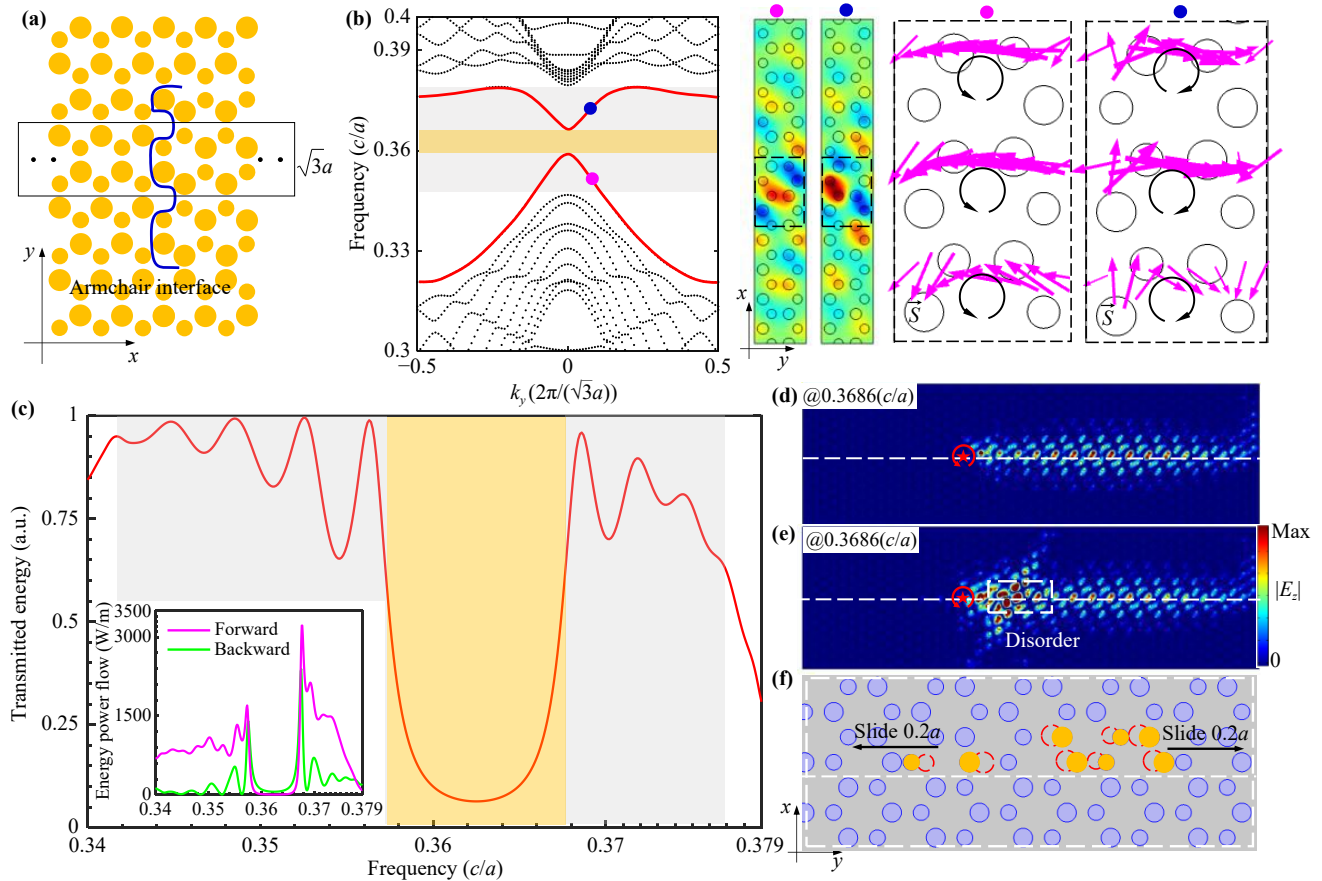


Fig. 3 Valley Hall edge states in the armchair interface. (a) Schematic of armchair interface, black rectangle denotes supercell. (b) The photonic bulk bands diagram along Γ -M momentum space. Light yellow shadow denotes completed PBG. Right panels: \mathbf{S} denotes Poynting vector marked by pink arrows, black circular arrows denote directions of energy power flow. (c) The transmission spectrum as a function of frequency in straight waveguide. Inset: Forward and backward energy flows through the vertical planes, respectively. (d, e) $|E_z|$ distributions of valley Hall edge states along the armchair interface and with disorder, the white dashed lines denote the interface. (f) Schematic diagram of the armchair interface with disorder. The red dashed circles show the original position without disorder. The yellow circles show the position of the cylinders after the move.

out from bulk bands due to breaking the crystal symmetry. The right panel of Fig. 2(b) displays the eigenmode profiles of the valley Hall edge states, which exhibit an odd symmetry with respect to the mid-horizontal plane. The EM wave energy that passes through the planes 1 and 2 [indicated by the white dashed lines in Fig. 2(d) and (e)] can be calculated by $U = 1/2 \int_V \text{Re}(\mathbf{E} \times \mathbf{H}^*) \cdot d\mathbf{l}$ [15, 16], from which we can define the percentage of transmitted energy as $U_2/(U_1+U_2)$ and the resulting transmission spectra are shown in Fig. 2(c). From which one can see that whatever waveguide structure is straight or Z-shaped, the valley Hall edge states exhibit highly unidirectional transmission in bandwidth marked by light shadow. By full wave simulation, we give out electric field amplitude ($|E_z|$) distributions of valley Hall edge states in straight and Z-shaped waveguides, respectively, as shown in Figs. 2(d) and (e). The valley Hall edge states propagate unidirectionally along the bearded interface-1 and traverse sharp bends without backscat-

tering when excited by a chiral left-handed circularly polarized (LCP) source. This observation directly demonstrates the robust transmission of these states, which is guaranteed by their topological protection. Similarly, for the case of $\delta = 1/11$ shown in Fig. 2(f), the lattice interface exhibits mirror-inverted symmetry. Consequently, the dispersion of the valley Hall edge states undergoes a flip with respect to the K and K' valleys, as presented in Fig. 2(g). The corresponding eigenmodes, displayed in the right panel of Fig. 2(g), are even symmetric with respect to the mid-horizontal plane. The transmission spectra within the PBG exhibit a similar trend, showing high unidirectional transmission over the operational bandwidth. Therefore, the bearded interface in VPCs is advantageous for integrated photonic waveguides and circuits.

Figure 3(b) presents the photonic band diagram for the armchair interface [Fig. 3(a)]. Within the PBG, two pairs of edge states dispersion curves are observed. Their

characteristics bear a notable similarity to those reported in the Wu–Hu model [13]. Since the armchair interface is parallel to the lattice Γ – M direction [53], the EM wave propagation is analyzed along the y -axis. Accordingly, the supercell periodicity is aligned with the wavevector ky direction in our numerical simulations. The emergence of two pairs of edge states dispersion curves within PBG can be attributed to the folding of the K and K' valleys onto each other when the band structure is projected along the ky direction [54]. Consequently, the edge states propagating along the armchair interface at a given Bloch momentum are valley-locking, inheriting properties from both the K and K' valleys.

We analyze the eigenmodes marked by pink and blue dots, which reveal that the electric field component E_z is concentrated at the armchair interface and decays exponentially away from it. The vortices in the energy flux (Poynting vectors) around the valleys are clearly visible. The energy flow, indicated by the pink arrows, exhibits anticlockwise (clockwise) rotation, as denoted by the black circular arrows, corresponding to the valley-spin up (down) states, respectively. Furthermore, in Fig. 3(b), the small gap highlighted in yellow, resulting from the repulsion between the two edge states, signifies coupling between them [13, 16, 54]. Figure 3(c) presents the transmission spectra of the valley Hall edge states along the armchair interface. These spectra demonstrate high unidirectional transmission within the frequency bandwidth indicated by the light shadow, while transmission is nearly absent within the tiny gap. This is further corroborated by the inset of Fig. 3(c), which plots the forward and backward energy fluxes through designated vertical planes. As shown, both fluxes approach zero within the gap. Finally, Fig. 3(d) confirms that the valley Hall edge states propagate unidirectionally along the armchair interface at a frequency of $0.3686(c/a)$. The valley Hall edge states can bypass intentionally introduced disorder and maintain unidirectional propagation along the armchair interface without back-reflection. This demonstrates their robust transmission against defects or disorder, as shown in Figs. 3(e) and (f). Notably, these edge states also exhibit strong self-guided transmission [55] along the zigzag interface (see the right boundary of the ribbon). Additionally, discussion and analysis of the valley Hall edge states at the zigzag and comb-like interfaces [56] are provided in the Supplementary Material.

4 U-shaped waveguide

Building upon the preceding discussion and analysis of valley Hall edge state dispersions at different interfaces, we construct a U-shaped waveguide structure composed of bearded interface-1, -2 and armchair interfaces. To analyze and predict the transmission characteristics of

the valley Hall edge states within this U-shaped waveguide, we compile a composite dispersion diagram [Fig. 4(a)] by integrating the data from Figs. 2(b), (g), and Fig. 3(b). Schematics of the U-shaped waveguide structure are presented in Figs. 4(b1)–(b4), where the pink, green, and red lines represent bearded interface-1, bearded interface-2, and the armchair interface, respectively, with black arrows indicating the propagation direction of the valley Hall edge states. Based on Fig. 4(a), we can deduce the following transport scenarios: At frequency f_1 , the valley Hall edge states propagate unidirectionally along bearded interface-2, the armchair interface, and bearded interface-1 in sequence, as illustrated in Fig. 4(b1). At frequency f_2 , however, the states propagate unidirectionally along bearded interface-1 and bearded interface-2 but are absent at the armchair interface. Consequently, the EM wave becomes localized and confined at bearded interface-2, marked by the dashed rectangle in Fig. 4(b2). This localization occurs because frequency f_2 lies within a tiny gap that does not support the transport of valley Hall edge states at the armchair interface [57]. The EM wave is thus reflected at the interface termination due to the reversal of its valley degree of freedom [58]. Based on this analysis, we predict that the EM wave localizes near the intersection of the interfaces, forming a photonic cavity. This localization originates from a momentum shift, which leads to energy confinement due to a momentum mismatch between backward and forward scattering processes. This mechanism is fundamentally distinct from the localization of chiral edge states, which is intrinsically based on the non-Hermitian skin effect [28]. At frequency f_3 , valley Hall edge states propagate unidirectionally along bearded interface-2 and the armchair interface but are absent at bearded interface-1. Consequently, after propagating along bearded interface-2, the states are localized at the armchair interface, as similarly illustrated in Fig. 4(b3). Furthermore, by altering the polarization direction of the chiral source, the propagation direction can be controlled. Based on valley-spin locking, the edge states can be made to propagate rightward along bearded interface-2 at frequency f_1 (or, in principle, at any of the three frequencies), as demonstrated in Fig. 4(b4). These results demonstrate that within the U-shaped waveguide, valley Hall edge states can not only be guided but also selectively confined or localized at specific interfaces in a frequency-dependent manner. This functionality, guiding and frequency-selective trapping, renders the structure analogous to a topological rainbow device [40].

The corresponding numerical simulation results at the respective frequencies are presented in Figs. 4(c1)–(c4). The $|E_z|$ field distributions of the valley Hall edge states observed in these figures are in full agreement with our previous analysis and predictions. Most notably, at frequency f_3 , a significantly enhanced electric field intensity

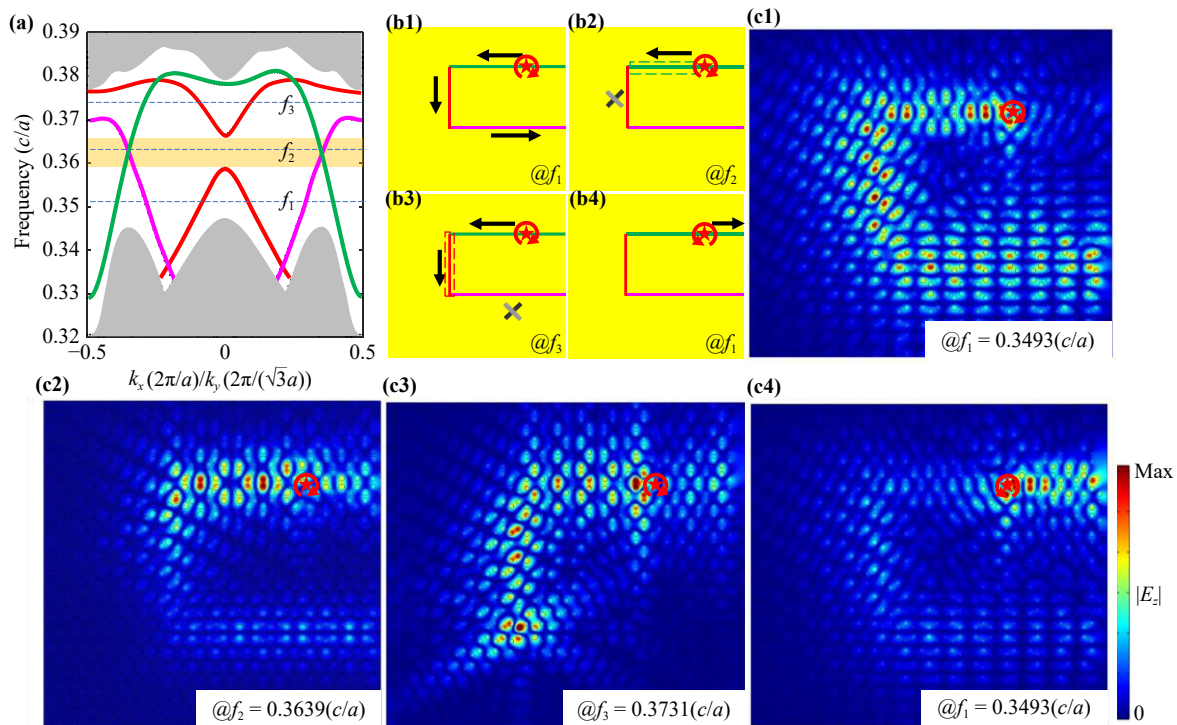


Fig. 4 U-shaped waveguide. **(a)** Valley Hall edge modes dispersion curves of the bearded interface-1, -2 and armchair interface, marked by pink, green and red curves respectively. **(b1–b4)** Schematic diagram of U-shaped waveguide, black arrows denote transport direction of the topological edge states, “×” denotes cannot support transport of valley Hall edge states in the interfaces. Where the pink, green and red lines represent the bearded interface-1, -2 and armchair interfaces respectively. The dashed rectangles represent localization zone of U-shaped waveguide. **(c1–c4)** $|E_z|$ distributions of U-shaped waveguide corresponding to (b1–b4) respectively.

is evident at the intersection between the armchair interface and bearded interface-1, as seen in Fig. 4(c3). This enhancement can be attributed to the mechanism discussed earlier: at the junction between two distinct interfaces, the valley Hall edge states undergo a “valley index flip” (from K to K’ or vice versa). During this flipping process, the effective reflection time (or delay time) for photon transmission is substantially prolonged. This extended delay, under the condition of near-conservation of the valley DOF [58], leads to the pronounced localization of photon energy at the interface termination. The numerical simulation results are in excellent agreement with the preceding predictions and analyses. Therefore, we have successfully demonstrated, theoretically, that the valley Hall edge states can be selectively localized at specific interfaces within the U-shaped waveguide through a frequency-dependent mechanism enabled by interface engineering. This operating principle, localizing states at predefined positions via their frequency, is functionally analogous to conventional topological rainbow trapping, where topological edge states of different frequencies are spatially separated and confined at distinct locations. However, a key advantage of our U-shaped waveguide design is its implementation simplicity: it requires neither modulation of an external

magnetic field, design of structures with gradually varying geometric parameters, nor the introduction of graded losses. Owing to these features, the interface-engineering-based U-shaped waveguide demonstrates significant potential for nanophotonic applications, such as robust light-harvesting devices [59] and ultra-compact topological rainbow nanolasers.

The experimental setup for the U-shaped waveguide is illustrated in Fig. 5(a). The configuration comprises three kinds of interfaces: bearded interface-2, the armchair interface, and bearded interface-1, highlighted by green, red, and pink lines, respectively. The fabricated sample consists of two distinct types of dielectric cylinders with radii of 0.3 mm and 0.25 mm, both having a height of 8 mm. This sample is positioned on a lower metallic plate (10 mm in height), together with an upper metallic plate, to form the complete waveguide device.

The microwave field mapper system [14, 16] is employed for measurement. A chiral source is inserted into the bottom plate via a drilled hole. The time-harmonic field distributions are then measured point-by-point using a probing antenna connected to a vector network analyzer (Keysight E5063A) through the top metallic plate. Experimentally, the electric field distributions along the interfaces of the U-shaped waveguide are

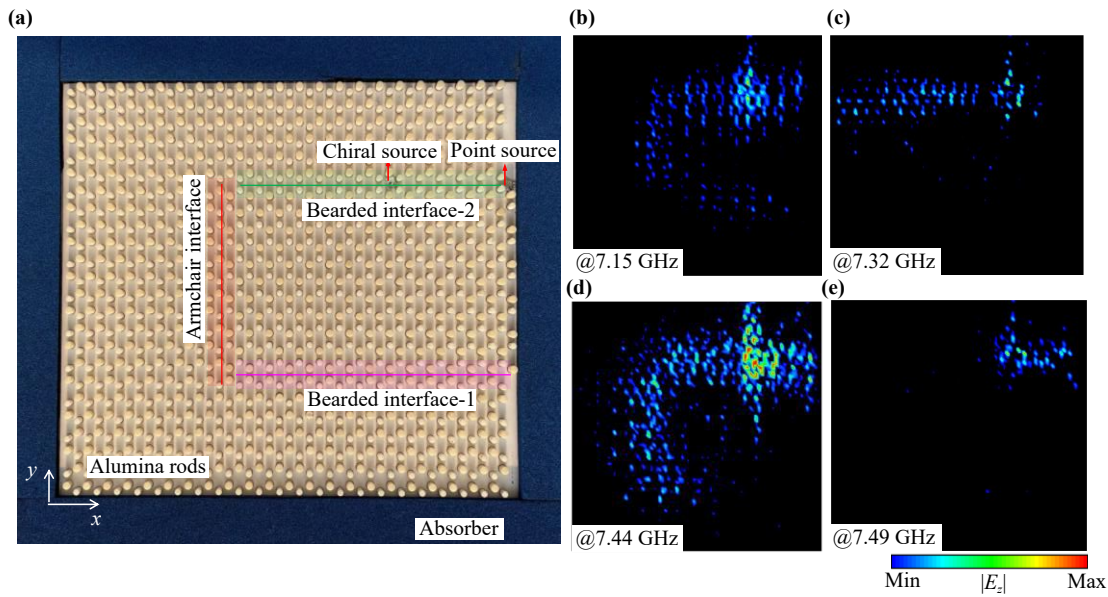


Fig. 5 Experimental observation of U-shaped waveguide. (a) Photograph of an experimental sample from top view. (b–e) Experimental observation for $|E_z|$ distributions of U-shaped waveguide corresponding to Figs. 4(c1)–(c4) respectively.

acquired by scanning the frequency within PBG in steps of 0.01 GHz, from which the electric field intensity profiles are derived. Consequently, a series of electric field intensity profiles at various frequencies are obtained. All experimental results are presented in Figs. 5(b)–(e), utilizing a chiral source as the excitation. Figure 5(b) demonstrates that at 7.15 GHz, the valley Hall edge states propagate unidirectionally along bearded interface-2, the armchair interface, and bearded interface-1, respectively. Similarly, at 7.32 GHz, the states propagate unidirectionally along bearded interface-2 and become localized at this interface, as shown in Fig. 5(c). Figure 5(d) shows that at 7.44 GHz, the unidirectional propagation occurs along bearded interface-2 and the armchair interface, with subsequent localization at the latter. Finally, when the chiral source is excited by left-handed circular polarization (RCP) at 7.49 GHz, the valley Hall edge states propagate rightward along bearded interface-2, as evidenced in Fig. 5(e). The experimental results clearly demonstrate that the U-shaped waveguide is selectively localized and confined at a specific interface in a frequency-dependent manner. Although a slight deviation exists between the numerical simulations and experimental measurements, which is acceptable and unavoidable owing to EM wave scattering in the experimental setup. Overall, the experimental results are in broad agreement with the numerical simulations. Detailed findings for the point source (dipole) excitation are provided in the Supplementary Material. For this configuration, EM wave scattering is comparatively weaker. While the results obtained from the dipole source show an offset relative to the previous experimental set, they remain in good agreement with the simulation

results.

Building upon the study of transmission characteristics for valley Hall edge states at different interfaces, we propose and demonstrate a potential application in integrated photonics and on-chip communications: topological metasurface antennas. By constructing distinct interfaces, these antennas can be engineered to realize various microwave antenna functions. A detailed discussion of the topological metasurface antennas is provided in the Supplementary Material.

5 Conclusion

In conclusion, we systematically and comprehensively study the valley Hall edge states at different interfaces in VPCs, including bearded (-1 and -2) and armchair interfaces. Building on the analysis of their transmission characteristics, we theoretically propose and experimentally demonstrate a U-shaped waveguide formed by these interfaces. The results confirm that the valley Hall edge states can not only guide but also be selectively confined or localized at a given interface within the waveguide, governed by frequency dependence. Moreover, compared to previous approaches, our fabrication method is simpler and more convenient, as it does not require complex techniques or additional processing steps. These findings provide a potential and viable platform for controlling EM waves by utilizing interfaces as an additional DOF at the nanoscale. For future work, it would be promising to experimentally extend this U-shaped waveguide concept to higher frequency regimes, such as terahertz, infrared, and optical bands, enabling more compact on-chip applications.



Declarations The authors declare that they have no competing interests and there are no conflicts.

Electronic supplementary material See the supplementary material for valley Hall edge states at different interfaces (i.e., comb-like interface, zigzag interface), and other experimental results at <https://doi.org/10.15302/frontphys.2026.103203>.

Acknowledgements This work was supported by the National Natural Science Foundation of China (Grant Nos. 62505298 and 12574477) and Zhejiang Provincial Natural Science Foundation of China (Grant No. LQN26F050010).

References

1. L. Lu, J. D. Joannopoulos, and M. Soljačić, Topological photonics, *Nat. Photonics* 8(11), 821 (2014)
2. A. B. Khanikaev and G. Shvets, Two-dimensional topological photonics, *Nat. Photonics* 11(12), 763 (2017)
3. T. Ozawa, H. M. Price, A. Amo, N. Goldman, M. Hafezi, L. Lu, M. C. Rechtsman, D. Schuster, J. Simon, O. Zilberberg, and I. Carusotto, Topological photonics, *Rev. Mod. Phys.* 91(1), 015006 (2019)
4. Z. H. Lan, M. L. N. Chen, F. Gao, S. Zhang, and W. E. I. Sha, A brief review of topological photonics in one, two, and three dimensions, *Rev. Phys.* 9, 100076 (2022)
5. J. W. You, Z. H. Lan, Q. Ma, Z. Gao, Y. Yang, F. Gao, M. Xiao, and T. J. Cui, Topological metasurface: From passive toward active and beyond, *Photon. Res.* 11(3), B65 (2023)
6. F. D. M. Haldane and S. Raghu, Possible realization of directional optical waveguides in photonic crystals with broken time-reversal symmetry, *Phys. Rev. Lett.* 100(1), 013904 (2008)
7. Z. Wang, Y. D. Chong, J. D. Joannopoulos, and M. Soljačić, Reflection-free one-way edge modes in a gyromagnetic photonic crystal, *Phys. Rev. Lett.* 100(1), 013905 (2008)
8. Z. Wang, Y. D. Chong, J. D. Joannopoulos, and M. Soljačić, Observation of unidirectional backscattering-immune topological electromagnetic states, *Nature* 461(7265), 772 (2009)
9. M. D. Wang, R. Y. Zhang, L. Zhang, D. Wang, Q. Guo, Z. Q. Zhang, and C. T. Chan, Topological one-way large-area waveguide states in magnetic photonic crystals, *Phys. Rev. Lett.* 126(6), 067401 (2021)
10. G. G. Liu, Z. Gao, Q. Wang, X. Xi, Y. H. Hu, M. Wang, C. Liu, X. Lin, L. Deng, S. A. Yang, P. Zhou, Y. Yang, Y. Chong, and B. Zhang, Topological Chern vectors in three-dimensional photonic crystals, *Nature* 609(7929), 925 (2022)
11. Z. T. Wu, Z. Y. Wang, Y. Meng, J. Chen, X. Xi, P. P. Shum, and Z. Gao, Realization of a chiral topological whispering-gallery-mode cavity in gyromagnetic photonic crystals, *Laser Photonics Rev.* 19(6), 2401451 (2025)
12. A. B. Khanikaev, S. Hossein Mousavi, W. K. Tse, M. Kargarian, A. H. MacDonald, and G. Shvets, Photonic topological insulators, *Nat. Mater.* 12(3), 233 (2013)
13. L. H. Wu and X. Hu, Scheme for achieving a topological photonic crystal by using dielectric material, *Phys. Rev. Lett.* 114(22), 223901 (2015)
14. Y. T. Yang, Y. F. Xu, T. Xu, H. X. Wang, J. H. Jiang, X. Hu, and Z. H. Hang, Visualization of a unidirectional electromagnetic waveguide using topological photonic crystals made of dielectric materials, *Phys. Rev. Lett.* 120(21), 217401 (2018)
15. L. He, Z. H. Lan, Y. T. Yang, Q. Ren, J. W. You, W. E. I. Sha, W. Liang, and J. Yao, Wavelength division multiplexing based on the coupling effect of helical edge states in two-dimensional dielectric photonic crystals, *Opt. Express* 32(7), 11259 (2024)
16. L. He, Z. H. Lan, B. Yang, J. Yao, Q. Ren, J. W. You, W. E. I. Sha, Y. Yang, and L. Wu, Experimental observation of topological large-area pseudospin-momentum-locking waveguide states with exceptional robustness, *Adv. Photon. Nexus* 3(1), 016009 (2024)
17. T. Ma and G. Shvets, All-Si valley-Hall photonic topological insulator, *New J. Phys.* 18(2), 025012 (2016)
18. X. D. Chen, F. L. Zhao, M. Chen, and J. W. Dong, Valley-contrasting physics in all-dielectric photonic crystals: Orbital angular momentum and topological propagation, *Phys. Rev. B* 96(2), 020202 (2017)
19. X. T. He, E. T. Liang, J. J. Yuan, H. Y. Qiu, X. D. Chen, F. L. Zhao, and J. W. Dong, A silicon-on insulator slab for topological valley transport, *Nat. Commun.* 10(1), 872 (2019)
20. C. A. Rosiek, G. Arregui, A. Vladimirova, M. Albrechtsen, B. Vosoughi Lahijani, R. E. Christiansen, and S. Stobbe, Observation of strong backscattering in valley-Hall photonic topological interface modes, *Nat. Photonics* 17(5), 386 (2023)
21. J. Li, R. L. Chu, J. K. Jain, and S. Q. Shen, Topological Anderson insulator, *Phys. Rev. Lett.* 102(13), 136806 (2009)
22. S. Stützer, Y. Plotnik, Y. Lumer, P. Titum, N. H. Lindner, M. Segev, M. C. Rechtsman, and A. Szameit, Photonic topological Anderson insulators, *Nature* 560(7719), 461 (2018)
23. G. G. Liu, Y. H. Yang, X. Ren, H. Xue, X. Lin, Y. H. Hu, H. Sun, B. Peng, P. Zhou, Y. Chong, and B. Zhang, Topological Anderson insulator in disordered photonic crystals, *Phys. Rev. Lett.* 125(13), 133603 (2020)
24. L. J. Maczewsky, J. M. Zeuner, S. Nolte, and A. Szameit, Observation of photonic anomalous Floquet topological insulators, *Nat. Commun.* 8(1), 13756 (2017)
25. G. G. Pyrialakos, J. Beck, M. Heinrich, L. J. Maczewsky, N. V. Kantartzis, M. Khajavikhan, A. Szameit, and D. N. Christodoulides, Bimorphic Floquet topological insulators, *Nat. Mater.* 21(6), 634 (2022)
26. X. Q. Zhao, J. J. Wang, W. Z. Liu, Z. Che, X. Wang, C. T. Chan, L. Shi, and J. Zi, Spin-orbit-locking chiral bound states in the continuum, *Phys. Rev. Lett.* 133(3), 036201 (2024)

27. Z. P. Gong, Y. Ashida, K. Kawabata, K. Takasan, S. Higashikawa, and M. Ueda, Topological phases of non-Hermitian systems, *Phys. Rev. X* 8(3), 031079 (2018)
28. G. G. Liu, S. Mandal, P. H. Zhou, X. Xi, R. Banerjee, Y. H. Hu, M. Wei, M. Wang, Q. Wang, Z. Gao, H. Chen, Y. Yang, Y. Chong, and B. Zhang, Localization of chiral edge states by the non-Hermitian skin effect, *Phys. Rev. Lett.* 132(11), 113802 (2024)
29. T. X. Dai, Y. T. Ao, J. Mao, Y. Yang, Y. Zheng, C. Zhai, Y. Li, J. Yuan, B. Tang, Z. Li, J. Luo, W. Wang, X. Hu, Q. Gong, and J. Wang, Non-Hermitian topological phase transitions controlled by nonlinearity, *Nat. Phys.* 20(1), 101 (2024)
30. Z. Tang, T. Chen, X. Tang, and X. D. Zhang, Topologically protected entanglement switching around exceptional points, *Light Sci. Appl.* 13(1), 167 (2024)
31. L. He, D. N. Liu, H. Z. Zhang, F. Zhang, W. Zhang, X. Feng, Y. Huang, K. Cui, F. Liu, W. Zhang, and X. Zhang, Topologically protected quantum logic gates with valley-Hall photonic crystals, *Adv. Mater.* 36(24), 2311611 (2024)
32. M. A. Bandres, S. Wittek, G. Harari, M. Parto, J. Ren, M. Segev, D. N. Christodoulides, and M. Khajavikhan, Topological insulator laser: experiments, *Science* 359(6381), eaar4005 (2018)
33. Y. Q. Zeng, U. Chattopadhyay, B. F. Zhu, B. Qiang, J. Li, Y. Jin, L. Li, A. G. Davies, E. H. Linfield, B. Zhang, Y. Chong, and Q. J. Wang, Electrically pumped topological laser with valley edge modes, *Nature* 578(7794), 246 (2020)
34. L. He and J. Q. Yao, Valley-Hall slow-light waveguide states with dual-band in all-dielectric valley photonic crystals, *Results Phys.* 68, 108092 (2025)
35. Y. H. Yang, Y. Yamagami, X. B. Yu, P. Pitchappa, J. Webber, B. Zhang, M. Fujita, T. Nagatsuma, and R. Singh, Terahertz topological photonics for on-chip communication, *Nat. Photonics* 14(7), 446 (2020)
36. R. D. Jia, S. Kumar, T. C. Tan, A. Kumar, Y. J. Tan, M. Gupta, P. Szriftgiser, A. Alphones, G. Ducournau, and R. Singh, Valley-conserved topological integrated antenna for 100-Gbps THz 6G wireless, *Sci. Adv.* 9(44), eadi8500 (2023)
37. A. Kumar, M. Gupta, P. Pitchappa, N. Wang, P. Szriftgiser, G. Ducournau, and R. Singh, Phototunable chip-scale topological photonics: 160 Gbps waveguide and demultiplexer for THz 6G communication, *Nat. Commun.* 13(1), 5404 (2022)
38. W. H. Wang, Y. J. Tan, T. C. Tan, A. Kumar, P. Pitchappa, P. Szriftgiser, G. Ducournau, and R. Singh, On-chip topological beamformer for multi-link terahertz 6G to XG wireless, *Nature* 632(8025), 522 (2024)
39. C. C. Lu, C. Y. Wang, M. Xiao, Z. Q. Zhang, and C. T. Chan, Topological rainbow concentrator based on synthetic dimension, *Phys. Rev. Lett.* 126(11), 113902 (2021)
40. W. Zhao, R. Zhou, and C. C. Lu, Research progress on topological rainbow, *Acta Opt. Sin.* 2(10), 1010001 (2025)
41. S. E. Soliman, M. Barlou, Z. J. Wong, and K. L. Tsakmakidis, Topological rainbow trapping, *Nat. Rev. Phys.* 7(8), 409 (2025)
42. S. E. Soliman, M. Barlou, K. L. Tsakmakidis, and Z. J. Wong, Rainbow trapping for advanced wave control, *Adv. Phys. X* 10(1), 2517551 (2025)
43. J. F. Chen, W. Y. Liang, and Z. Y. Li, Switchable slow light rainbow trapping and releasing in strongly coupling topological photonic systems, *Photon. Res.* 7(9), 1075 (2019)
44. C. C. Lu, Y. Z. Sun, C. Y. Wang, H. Zhang, W. Zhao, X. Hu, M. Xiao, W. Ding, Y. C. Liu, and C. T. Chan, On-chip nanophotonic topological rainbow, *Nat. Commun.* 13(1), 2586 (2022)
45. C. C. Lu, W. Zhao, S. Zhang, Y. Zheng, C. Wang, Y. Li, Y. C. Liu, X. Hu, and Z. Hong Hang, Observation of topological rainbow in non-Hermitian systems, *Chin. Opt. Lett.* 21(12), 123601 (2023)
46. D. Yu, S. Arora, and L. Kuipers, Impact of transforming interface geometry on edge states in valley photonic crystals, *Phys. Rev. Lett.* 132(11), 116901 (2024)
47. R. D. Jia, Y. J. Tan, N. Navaratna, A. Kumar, and R. Singh, Photonic supercoupling in silicon topological waveguides, *Adv. Mater.* 37(6), 2415083 (2025)
48. Y. Plotnik, M. C. Rechtsman, D. H. Song, M. Heinrich, J. M. Zeuner, S. Nolte, Y. Lumer, N. Malkova, J. Xu, A. Szameit, Z. Chen, and M. Segev, Observation of unconventional edge states in ‘photonic graphene’, *Nat. Mater.* 13(1), 57 (2014)
49. W. S. Ruan, X. T. He, F. L. Zhao, and J. W. Dong, Analysis of unidirectional coupling in topological valley photonic crystal waveguides, *J. Lightwave Technol.* 39(4), 889 (2021)
50. J. J. Ma, C. Ouyang, Y. T. Yang, D. Wang, H. Li, L. Niu, Y. Liu, Q. Xu, Y. Li, Z. Tian, J. Han, and W. Zhang, Asymmetric frequency multiplexing topological devices based on a floating edge band, *Photon. Res.* 12(6), 1201 (2024)
51. F. Tian, Y. Wang, W. Huang, X. Fang, S. Guo, and T. Zhou, Ultra-compact topological photonic crystal rainbow nanolasers operating in the 1550 nm telecom band with wavelength-scale mode volumes, *Adv. Mater.* 37(45), e05699 (2025)
52. G. M. Graf and M. Porta, Bulk-edge correspondence for two dimensional topological insulators, *Commun. Math. Phys.* 324(3), 851 (2013)
53. T. W. Liu and F. Semperlotti, Experimental evidence of robust acoustic valley Hall edge states in a nonresonant topological elastic waveguide, *Phys. Rev. Appl.* 11(1), 014040 (2019)
54. Q. Tang, M. R. Belic, Y. Q. Zhang, Y. P. Zhang, and Y. D. Li, Valley Hall edge solitons in honeycomb lattice with an armchair-type domain wall, *Nonlinear Dyn.* 108(2), 1573 (2022)
55. Y. Poo, R. X. Wu, Z. F. Lin, Y. Yang, and C. T. Chan, Experimental realization of self-guiding unidirectional electromagnetic edge states, *Phys. Rev. Lett.* 106(9), 093903 (2011)



56. Z. P. Qi, G. H. Hu, C. Y. Deng, H. Sun, Y. Sun, Y. Li, B. Liu, Y. Bai, S. Chen, and Y. Cui, Electrical tunable topological valley photonic crystals for on-chip optical communications in the telecom band, *Nanophotonics* 11(18), 4273 (2022)
57. Y. T. Yang, X. Qian, L. Shi, X. Shen, Y. Wang, and Z. H. Hang, Observation and control of pseudospin switching in a finite-width topological photonic crystal, *Opt. Express* 30(4), 5731 (2022)
58. Y. D. Li, Y. Yu, F. Y. Liu, B. Zhang, and G. Shvets, Topology-controlled photonic cavity based on the near-conservation of the valley degree of freedom, *Phys. Rev. Lett.* 125(21), 213902 (2020)
59. S. Weidemann, M. Kremer, T. Helbig, T. Hofmann, A. Stegmaier, M. Greiter, R. Thomale, and A. Szameit, Topological funneling of light, *Science* 368(6488), 311 (2020)